JASA ARTICLE

Injection of acoustic waves via volumetric sources on a control surface for computational aeroacoustics

Giovanni Coco,[1,2,a] Didier Dragna,[1] Christophe Bailly,[1] and Hélène Posson[2]
[1]*École Centrale de Lyon, Centre National de la Recherche Scientifique, Université Claude Bernard Lyon 1, Institut National des Sciences Appliquées de Lyon, Laboratoire de Mécanique des Fluides et d'Acoustique, Unité Mixte de Recherche 5509, 69130 Écully, France*
[2]*Safran Aircraft Engines, Rond Point René Ravaud–Réau, 77550 Moissy-Cramayel, France*

ABSTRACT:
A formulation to introduce acoustic waves from a control surface using volumetric source terms is proposed for numerical simulations. A general expression of the source terms is derived from the non-linear Euler equations. The method is validated through three academic configurations: the injection of oblique plane waves and the radiation of a monopole source in two and three dimensions, in uniform flow. The governing equations are solved in a Cartesian grid using a low-dispersion and low-dissipation high order finite-difference numerical scheme. However, the control surface has an arbitrary shape, as demonstrated here with the use of a cylindrical surface. Numerical results show good agreement with analytical solutions in both phase and amplitude. The method is then applied to an open-fan aircraft engine configuration. The source terms are computed from a cylindrical control surface enclosing the rotor, based on data extracted from a previous fluid mechanics simulation. The radiated acoustic field is compared with the one obtained using the Ffowcs Williams–Hawkings integral formulation. The two solutions are again found in good agreement for this more realistic configuration.
https://doi.org/10.1121/10.0042388
(Received 24 July 2025; revised 21 December 2025; accepted 14 January 2026; published online 5 February 2026)
[Editor: Xun Huang] Pages: 1151–1162

I. INTRODUCTION

Prescribing incoming pressure and velocity perturbations without generating spurious waves is always a tricky subject in computational aeroacoustics.[1] This is all the more true when the time-dependent signal to be injected is extracted from a separate numerical simulation in fluid mechanics. The aim of the present study is to be able to solve the full Euler equations to take account of possible non-linear propagation effects in the presence of a mean flow, by forcing the system with a solution of the averaged Navier-Stokes equations around an open rotor.

Several strategies have been proposed in the literature to address this coupling. One of the most widely adopted approach is the Ffowcs Williams–Hawkings[2] integral method. By enclosing the acoustic source within a porous control surface, equivalent source terms are derived to solve the wave equation in the farfield. While effective for linear propagation in a homogeneous medium, this method does not account for non-linear effects[3] or the presence of physical obstacles within the extrapolation domain.

An alternative strategy relies on the direct use of acoustic data on a control surface. Perturbations can be imposed explicitly, as done by de Cacqueray *et al.*[4] to characterize non-linear propagation effects of supersonic jet noise and Emmanuelli *et al.*[5] to prescribe the incoming non-linear acoustic wave at the computational domain inlet. A formal two-way coupling between two solvers can also be used for more complex computational domains, as investigated by Langenais *et al.*[6] for noise on a launch pad.

The method of characteristics, first developed by Thompson[7,8] and generalized by Poinsot and Lele[9] with the Navier-Stokes characteristic boundary conditions method, provides an alternative approach for enforcing boundary conditions. The method was further improved by Daviller *et al.*[10] to prevent divergence of the mean inlet velocity from the target value, enabling accurate introduction of both turbulent and acoustic velocity components. The method of characteristics was used by Daroukh *et al.*,[11] for instance, as a computational fluids dynamics–Euler coupling strategy to introduce acoustic waves. A mesh conforming to the surface geometry is in general used. Moreover, the method of characteristics is inherently one-dimensional and performs optimally only when the acoustic wave vector is normal to the injection surface.[12,13]

A different approach based on volumetric source terms distributed over a surface surrounding the acoustic source is followed in the present work. Initial developments by Maeda and Colonius[14] proposed a framework to generate one-way acoustic waves using a linear combination of monopole and dipole sources on a surface. Their model, however, is limited to quiescent media and based on a one-dimensional formulation. The present work extends this concept by formulating source terms for the non-linear Euler equations, enabling the introduction of waves from arbitrarily shaped surfaces in the presence of a mean flow and taking into account non-linear effects.

[a]Email: giovanni.coco@ec-lyon.fr

The text is organized as follows. Section II introduces the methodological framework and details the derivation of the source terms. Section III describes the numerical setup used in the simulations. Section IV presents the results across four representative academic configurations including a realistic coupling for the last case. Final remarks and conclusions are drawn in Sec. V.

II. FORMULATION

A spatial domain Ω containing an acoustic source region is considered, as shown in Fig. 1. An arbitrary stationary control volume V is defined such that the source region lies within it. The outer boundary of this volume is a permeable surface described by the zero level set of a scalar function $f(\mathbf{x}) = 0$, with $f < 0$ in V and $f > 0$ outside V. The set of points describing the surface is denoted $\mathbf{x_s}$, with thus $f(\mathbf{x_s}) = 0$. The surface equation is constructed so that its gradient satisfies $|\nabla f(\mathbf{x_s})| = 1$. In addition, we introduce $\boldsymbol{n} = \nabla f(\mathbf{x_s})$ the unit normal vector to the surface.

The non-linear Euler equations written in a perturbative form are solved throughout the whole domain Ω,

$$\frac{\partial \rho}{\partial t} + \frac{\partial}{\partial x_i}(\rho u_i - \rho_0 u_{0_i}) = 0, \tag{1}$$

$$\frac{\partial}{\partial t}(\rho u_i) + \frac{\partial}{\partial x_j}(\rho u_i u_j - \rho_0 u_{0_i} u_{0_j}) + \frac{\partial}{\partial x_i}(p - p_0) = 0, \tag{2}$$

$$\frac{\partial}{\partial t}(\rho e_t) + \frac{\partial}{\partial x_i}[u_i(\rho e_t + p) - u_{0_i}((\rho e_t)_0 + p_0)] = 0, \tag{3}$$

where ρ is density, t is time, x_i is the spatial coordinate along the i-direction, u_i is the component along the i-direction of the velocity vector $\mathbf{u}$, and p is the pressure. Finally, e_t is the total energy per mass unit, given by

$$\rho e_t = \frac{p}{\gamma - 1} + \frac{1}{2}\rho u_i^2 \tag{4}$$

for a perfect gas, with γ the ratio of specific heats set to 1.4. Equation (4) is then used to calculate p. The notation $(\cdot)_0$ denotes the base flow quantities, assumed to be known as the governing equations are formulated exclusively for perturbations.

Similarly to the strategy of the Ffowcs Williams & Hawkings (FWH) analogy,[2] Eqs. (1), (2), and (3) are then multiplied by the Heaviside function applied to the surface $H(f)$, and the source terms are identified by isolating the resulting right-hand side contributions.

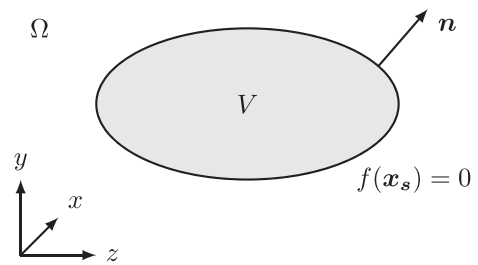

FIG. 1. Spatial domain Ω containing a control volume V. The surface enclosing V is denoted by $f(\mathbf{x_s}) = 0$, and $\boldsymbol{n}$ the unit normal vector.

For the mass conservation equation, this gives

$$H(f)\left[\frac{\partial \rho}{\partial t} + \frac{\partial}{\partial x_i}(\rho u_i - \rho_0 u_{0_i})\right] = 0, \tag{5}$$

which can be rewritten as

$$\frac{\partial}{\partial t}[\rho H(f)] + \frac{\partial}{\partial x_i}\left[(\rho u_i - \rho_0 u_{0_i})H(f)\right] = (\rho u_i - \rho_0 u_{0_i})\frac{\partial H(f)}{\partial x_i}. \tag{6}$$

We have used the relation

$$\frac{\partial H(f)}{\partial x_i} = \frac{\partial H(f)}{\partial f}\frac{\partial f}{\partial x_i} = \delta(f)\ n_i, \tag{7}$$

where $\delta(f)$ is the Dirac delta function applied to f, and n_i is the normal vector component along the i-direction. Introducing Eq. (7) into Eq. (6) leads to

$$\frac{\partial}{\partial t}[\rho H(f)] + \frac{\partial}{\partial x_i}\left[(\rho u_i - \rho_0 u_{0_i})H(f)\right] = \Lambda_\rho, \tag{8}$$

where the source term reads as

$$\Lambda_\rho = (\rho \mathbf{u} - \rho_0 \mathbf{u_0}) \cdot \mathbf{n}\ \delta(f). \tag{9}$$

Note that the terms on the left-hand side of Eq. (8) correspond to the field solved outside the control surface, that is Eq. (1) written for the variable $\rho H(f)$, while the remaining terms are identified as source terms on the right-hand side. The same methodology applied to the momentum and energy conservation equations provides

$$\frac{\partial}{\partial t}[\rho u_i H(f)] + \frac{\partial}{\partial x_j}\left[(\rho u_i u_j - \rho_0 u_{0_i} u_{0_j})H(f)\right] + \frac{\partial}{\partial x_i}\left[(p - p_0)H(f)\right] = \Lambda_{\rho \boldsymbol{u}}, \tag{10}$$

$$\frac{\partial}{\partial t}[\rho e_t H(f)] + \frac{\partial}{\partial x_i}\left\{[u_i(\rho e_t + p) - u_{0_i}((\rho e_t)_0 + p_0)]H(f)\right\} = \Lambda_{\rho e_t} \tag{11}$$

with the source terms

$$\Lambda_{\rho \boldsymbol{u}} = [\rho(\mathbf{u}\cdot\mathbf{n})\mathbf{u} - \rho_0(\mathbf{u_0}\cdot\mathbf{n})\mathbf{u_0} + (p - p_0)\ \mathbf{n}]\ \delta(f), \tag{12}$$

$$\Lambda_{\rho e_t} = \left[(\rho e_t + p)\mathbf{u} - ((\rho e_t)_0 + p_0)\mathbf{u_0}\right] \cdot \mathbf{n}\ \delta(f). \tag{13}$$

The three newfound source terms at the right-hand side in Eqs. (8), (10), and (11), Λ_ρ, $\Lambda_{\rho \boldsymbol{u}}$, and $\Lambda_{\rho e_t}$, are, respectively, the sources terms for mass, momentum, and energy conservation equations. These sources are continuously distributed along the entire control surface. They enable the

https://doi.org/10.1121/10.0042388

signal generated by the source region within the volume V to be injected into the computational domain in the outward direction only. No propagation should be observed in the volume V.

III. NUMERICAL SETUP

The Euler equations are solved in their conservative form written in Cartesian coordinates

$$\frac{\partial \boldsymbol{U}}{\partial t}+\frac{\partial \boldsymbol{E}}{\partial x}+\frac{\partial \boldsymbol{F}}{\partial y}+\frac{\partial \boldsymbol{G}}{\partial z}=\Lambda, \tag{14}$$

with

$$\begin{aligned}
\boldsymbol{U} &= (\rho, \rho u, \rho v, \rho w, \rho e_t),\\
\boldsymbol{E} &= \big(\rho u, \rho u^2, \rho uv, \rho uw, u(\rho e_t + p)\big),\\
\boldsymbol{F} &= \big(\rho v, \rho uv, \rho v^2, \rho vw, v(\rho e_t + p)\big),\\
\boldsymbol{G} &= \big(\rho w, \rho uw, \rho vw, \rho w^2, w(\rho e_t + p)\big),\\
\Lambda &= (\Lambda_\rho, \Lambda_{\rho u}, \Lambda_{\rho v}, \Lambda_{\rho w}, \Lambda_{\rho e_t}),
\end{aligned}$$

where $\boldsymbol{U}$ is the vector of conservative variables, $\boldsymbol{E}, \boldsymbol{F}$, and $\boldsymbol{G}$ are the fluxes vectors, Λ is the source term vector defined in Eqs. (9), (12), and (13) over $f(\boldsymbol{x}_s)=0$, $\boldsymbol{x}=(x,y,z)$, and $\boldsymbol{u}=(u,v,w)$. As mentioned previously, Eq. (14) is solved for perturbative variables with respect to a given based flow. The variables are initialized with their ambient values, that is $\boldsymbol{U}(\mathbf{x}, t=0)=(\rho_0, \rho_0 u_0, \rho_0 v_0, \rho_0 w_0, (\rho e_t)_0)$.

The Euler equations are solved using a finite difference approach in a uniformly spaced Cartesian grid, i.e., $\Delta x=\Delta y=\Delta z$, where Δx, Δy, Δz are the grid sizes in the x-, y-, and z-direction, respectively. Spatial derivatives are computed with a low dispersion and low dissipation fourth-order, 11-point finite difference scheme.[15] Temporal integration is performed using a low-storage, fourth-order, six-stage Runge–Kutta scheme. The source terms are introduced at the last substep of each iteration of the temporal scheme. This choice was made with the open-fan application presented in Sec. IV D in mind, where the input signal is obtained from a RANS simulation and is not analytically defined. A selective 11-point filter is applied throughout the computational domain in order to suppress grid-to-grid oscillations. Perfectly matched layers (PML)[16] are implemented near the domain boundaries to absorb outgoing acoustic waves. All simulations are conducted with a Courant–Friedrichs–Lewy (CFL) number set to 0.5.

The source terms involve a Dirac delta function that has to be approximated for discretization. For that, we use a normalized Gaussian-shaped spatial support defined by

$$\delta_b[f(\boldsymbol{x})]=\frac{1}{\sqrt{\pi}b}\exp\left(-\frac{f(\boldsymbol{x})^2}{b^2}\right) \tag{15}$$

with $b=b_w/\sqrt{\log 2}$, where b_w is the Gaussian half-width. It can be remarked that δ_b tends to the Dirac function δ when b tends to zero. In the following, $b_w/\Delta x=1$ is chosen to ensure that the sources remain compact. Choosing $b_w/\Delta x<1$ may lead to numerical instability and increased error, whereas selecting a value that is too large spreads the sources intensity over a wider region, also increasing numerical error.

It should also be noted that approximating the Dirac delta function transforms the source terms from a surface distribution to a volumetric one, spread over the surface. The imposed acoustic fields have also to be extended from the control surface to the volumetric source. For that, we keep the same values along the direction normal to the surface. In other words, the width size of the source is assumed to be small with respect to a typical acoustic wavelength.

IV. RESULTS

Four configurations are presented to assess the methodology. The first case involves the injection of an oblique plane wave. The second and third cases consider the injection of cylindrical and spherical waves generated by a monopole in a uniform mean flow. The fourth applies to an open-fan configuration representative of a more realistic scenario. In the present methodology, acoustic waves are introduced by imposing the acoustic field on a predefined injection surface. For the first three academic cases, this field is specified analytically; in the fourth, it is obtained from a previous computational fluid dynamics simulation.

A perfect gas is considered, and p_0, ρ_0, and c_0 denote the pressure, density, and speed of sound of the medium at rest. For the first three academic cases, all the variables are made dimensionless with the speed of sound c_0 as velocity scale, ρ_0/γ as density scale, $\rho_0 c_0^2$ as pressure scale, an arbitrary length L, and a time scale L/c_0. The reported results are, however, plotted with dimensional primitive variables for the time and spatial coordinates. For the last case D, all variables carry physical dimensions.

Also, to clearly separate the quantities in the Euler equations from those imposed in the source terms, the latter are indicated in the following with a tilde ($\tilde{}$).

A. Oblique plane waves

The objective of the first problem is to introduce an oblique plane wave propagating at an angle θ with respect to the horizontal x axis in a medium at rest. The injection domain is defined by $f(x,y)=x$ [corresponding to $\boldsymbol{x}_s=(0,y)$], that is along a vertical line as illustrated in Fig. 2. The acoustic pressure $\tilde{p}'$ and acoustic velocity $\tilde{\boldsymbol{u}}'$ for an oblique plane wave read

$$\tilde{p}'(x,y,t)=A\cos\left[\omega\left(t-\frac{x}{c_0}\cos\theta-\frac{y}{c_0}\sin\theta\right)\right], \tag{16}$$

$$\tilde{\boldsymbol{u}}'(x,y,t)=\frac{A}{\rho_0 c_0}\cos\left[\omega\left(t-\frac{x}{c_0}\cos\theta-\frac{y}{c_0}\sin\theta\right)\right]\boldsymbol{v}, \tag{17}$$

where A denotes the wave amplitude and is set to 10^{-4} to be in the linear regime, ω is the angular frequency set to π, and $\boldsymbol{v}=(\cos\theta, \sin\theta)$ is the unit wave vector.

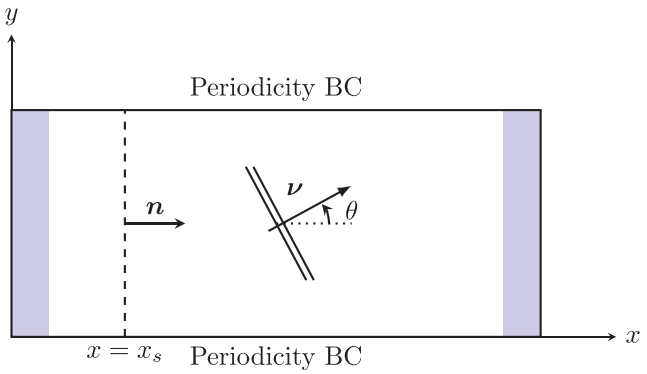

FIG. 2. Two-dimensional domain used to simulate oblique waves introduced along the vertical line $x = x_s$, with wave vector $\boldsymbol{\nu}$ inclined at an angle θ relative to the horizontal x axis. Blue regions at the left and right boundaries represent the PML, while periodic boundary conditions are applied along the top and bottom edges.

For this first case, small amplitude waves are considered to derive an analytical solution. The expressions of the source terms to be placed on the vertical line at $x = 0$ are determined by using Eqs. (9), (12), and (13). They are thus linearized in neglecting second order terms. By noting that the unit vector normal to the injection line is $\boldsymbol{n} = (1, 0)$, this gives

$$\Lambda_\rho(\boldsymbol{x}, t) = \rho_0 \tilde{u}'(\boldsymbol{x_s}, t)\ \ \delta_b(f), \tag{18}$$

$$\Lambda_{\rho u}(\boldsymbol{x}, t) = \tilde{p}'(\boldsymbol{x_s}, t)\ \ \delta_b(f), \tag{19}$$

$$\Lambda_{\rho v}(\boldsymbol{x}, t) = 0, \tag{20}$$

$$\Lambda_{\rho e_t}(\boldsymbol{x}, t) = \frac{\gamma}{\gamma - 1} p_0 \tilde{u}'(\boldsymbol{x_s}, t)\ \ \delta_b(f). \tag{21}$$

It can be shown analytically that the source terms given in Eqs. (18)–(21) generate an oblique plane wave whose properties match those in Eq. (16). To demonstrate this, the Euler equations are manipulated by following Maeda and Colonius[14] to recast them into the form of a wave equation

$$\frac{1}{c_0^2}\frac{\partial^2 p'}{\partial t^2} - \nabla^2 p' = S, \tag{22}$$

where the right-hand side reads

$$S = \frac{\partial \Lambda_\rho}{\partial t} - \nabla \cdot \boldsymbol{\Lambda_{\rho u}}. \tag{23}$$

The pressure field is then calculated by carrying out the convolution between the source term S and the free-space Green function $g_0(x, y, z, t)$,

$$p'(x, y, t) = (g_0 * S), \tag{24}$$

which leads for $|x| \gg b$ to

$$p' = A_b H(x) \cos\left[\omega\left(t - \frac{x}{c_0}\cos\theta - \frac{y}{c_0}\sin\theta\right)\right] \tag{25}$$

with

$$A_b = A \exp\left(-\frac{k_0^2 b^2 \cos\theta^2}{4}\right) \tag{26}$$

and $k_0 = \omega/c_0$. Providing that $k_0 b$ is sufficiently small, the acoustic pressure field corresponds to that for the propagation of the oblique plane wave in Eq. (16) for $x > 0$. In addition, it is found that the acoustic pressure field is null for $x < 0$. Details on the calculation of the convolution are given in Appendix A.

For numerical simulations, the grid spacing is set to $\Delta x = 0.05$, providing 44 points per wavelength. The computational domain consists of 401×201 points in the x and y directions, respectively. The length of the computational domain is selected to match the y-wise periodicity described in Eqs. (16) and (17). As shown in Fig. 2, PML are applied at the left and right boundaries, while periodic boundary conditions are imposed on the top and bottom edges. The solution is computed up to $t = 50$.

A snapshot of the acoustic pressure field is shown in Fig. 3. As expected, wave propagation is confined to the direction of increasing x, while the signal in the opposite direction remains at least three orders of magnitude lower. The time evolution of the acoustic pressure field is shown in Mm. 1.

Mm. 1. Evolution of the pressure field for an oblique wave train injected along a vertical line.

A comparison between the analytical and numerical solutions at the final time step, evaluated along the horizontal line $y = 3$, is plotted in Fig. 4. An excellent agreement is observed in both phase and amplitude. Beyond $x = 17$, the PML applied at the right boundary progressively attenuates the numerical solution to zero.

B. 2D Monopole with uniform mean flow

This second case aims at injecting cylindrical waves generated by a monopole immersed in a two-dimensional uniform base flow along the y axis, with a Mach number $M_y = v_0/c_0 = 0.8$.

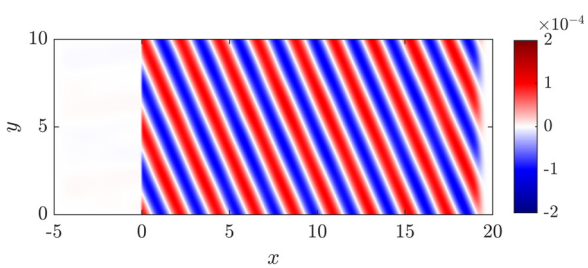

FIG. 3. Snapshot of the pressure field at $t = 50$ generated by the source terms located at $x = 0$. The wave propagates in the positive x-direction, while only a negligible amplitude is observed in the opposite direction.

https://doi.org/10.1121/10.0042388

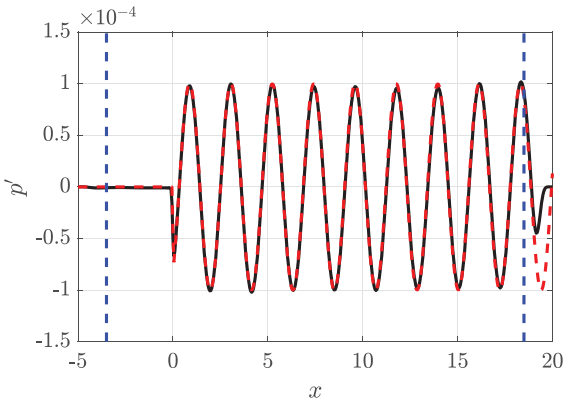

FIG. 4. Comparison between the analytical solution (dashed red line) and the numerical solution (solid black line) along the horizontal line $y = 3$.

As shown in Fig. 5, the control surface is a circle centered at the origin of the domain and with a radius $R_s = 5$. Its surface equation is $f(x,y) = \sqrt{x^2+y^2} - R_s$, corresponding to $\boldsymbol{x_s} = (R_s\cos\theta, R_s\sin\theta)$ with θ between 0 and 2π. The monopole position (x_m, y_m) does not coincide with the center of the control surface. The normal vector to the control surface is defined as

$$\boldsymbol{n} = \begin{pmatrix} n_x \\ n_y \end{pmatrix} = \begin{pmatrix} \cos\theta \\ \sin\theta \end{pmatrix}, \tag{27}$$

where n_x and n_y denote the components of the normal vector in the x- and y-directions, respectively, and θ is the angle formed with the horizontal x axis.

In complex notation, the acoustic pressure field generated by a monopole immersed in a uniform flow reads

$$\tilde{p}'(x,y,t) = -\rho_0\left(\frac{\partial}{\partial t} + v_0\frac{\partial}{\partial y}\right)\phi(x,y,t), \tag{28}$$

where $\phi(x,y,t)$ is the velocity potential defined as

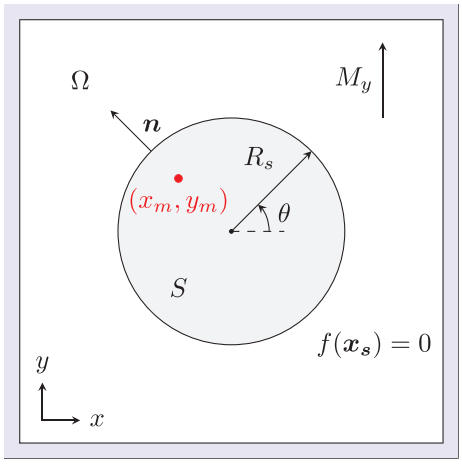

FIG. 5. Two-dimensional computational domain Ω, featuring a circular control surface $S \in \Omega$ centered at the origin with radius R_s. The acoustic monopole (in red) is located at (x_m, y_m) within the control surface. The blue region denotes the PML used for wave absorption.

$$\phi(x,y,t) = -\frac{iA}{4\beta}H_0^{(1)}\left(\frac{k_0}{\beta}\sqrt{(x-x_m)^2 + \frac{(y-y_m)^2}{\beta^2}}\right) \times \exp\left(-\frac{ik_0M_y}{\beta^2}(y-y_m)\right)\exp(-i\omega t).$$

In the above equation, $H_0^{(1)}$ is the Hankel function of the first kind, $\beta = (1-M_y^2)^{1/2}$ is the Prandtl–Glauert factor and A is the source amplitude. The acoustic density is simply given by $\tilde{\rho}'(\boldsymbol{x},t) = \tilde{p}'(\boldsymbol{x},t)/c_0^2$ and the acoustic velocity field is $\tilde{\boldsymbol{u}}' = \nabla\phi$.

Equations (9), (12), and (13) are again used to derive the source terms,

$$\Lambda_\rho(\boldsymbol{x},t) = \left(\rho_0\tilde{u}_n' + \tilde{\rho}'v_0\sin\theta\right)\ \delta_b(f), \tag{29}$$

$$\Lambda_{\rho u}(\boldsymbol{x},t) = \left(\rho_0v_0\tilde{u}'\sin\theta + \tilde{p}'\cos\theta\right)\ \delta_b(f), \tag{30}$$

$$\Lambda_{\rho v}(\boldsymbol{x},t) = \left(\rho_0v_0\tilde{u}_n' + \rho_0v_0\tilde{v}'\sin\theta + \tilde{\rho}'v_0^2\sin\theta + \tilde{p}'\sin\theta\right)\ \delta_b(f), \tag{31}$$

$$\Lambda_{\rho e_t}(\boldsymbol{x},t) = \left[\left(\frac{\gamma p_0}{\gamma-1} + \frac{1}{2}\rho_0v_0^2\right)\tilde{u}_n' + \frac{\gamma}{\gamma-1}v_0\tilde{p}'\sin\theta + \rho_0v_0^2\tilde{v}'\sin\theta + \frac{1}{2}v_0^3\tilde{\rho}'\sin\theta\right]\ \delta_b(f), \tag{32}$$

where $\tilde{u}_n'$ denotes the velocity component normal to the surface f, namely, $\tilde{u}_n' = \tilde{\boldsymbol{u}}'\cdot\boldsymbol{n} = \tilde{u}'\cos\theta + \tilde{v}'\sin\theta$. All the acoustic quantities are obtained by taking the real part of the analytical field evaluated at $(R_s\cos\theta, R_s\sin\theta, t)$. As a reminder, the values of the imposed acoustic quantities along the direction normal to the control surface are set equal to those on the surface. For this case, this implies that $\tilde{p}'$, $\tilde{u}'$, $\tilde{v}'$, and $\tilde{\rho}'$ are constant for a given value of θ.

The source amplitude A is set to 10^{-3} and the angular frequency $\omega = 0.1$. The grid spacing is set to $\Delta x = 0.1$, providing 150 points per wavelength in the upstream-propagating wave region. The computational domain consists of 1001×1001 points in the x and y directions, respectively. The solution is computed up to $t = 300$.

A snapshot of the pressure field is shown in Fig. 6 and the time evolution of the pressure fluctuation field can be observed in Mm. 2.

Mm. 2. Evolution of the pressure field for a two-dimensional monopole enclosed in a circular surface.

The circular control surface is centered at the origin of the computational domain, while the monopole, marked by a red cross, is located at $(x_m, y_m) = (3,3)$. The resulting acoustic wavefronts are clearly visible and exhibit asymmetry due to the convective effects of the mean flow. A quantitative comparison between the numerical and analytical solutions along six distinct lines is provided in Fig. 7, demonstrating excellent agreement in both amplitude and phase. For the lines $y = 0$ and $x = 0$, shown in Figs. 7(b) and 7(c),

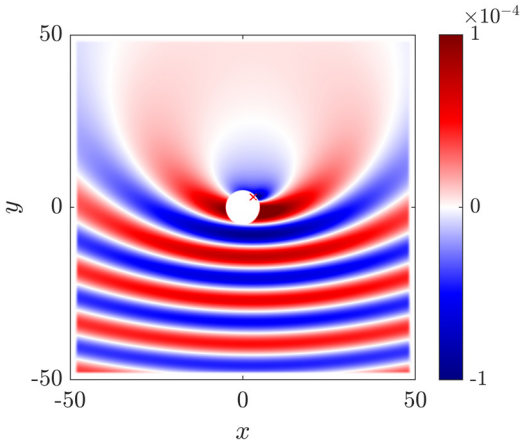

FIG. 6. Acoustic pressure field at $t = 300$ generated by a two-dimensional monopole immersed in a uniform flow with Mach number $M_y = 0.8$. The monopole, indicated by the red cross, is located at $(x_m, y_m) = (3, 3)$ within a circular control surface centered at the origin with radius $R_s = 5$.

respectively, a discontinuity appears for $x, y \in (-5, 5)$, corresponding to the region enclosed by the control surface. Within this region, no acoustic wave is introduced, a property of the present formulation.

A convergence study is carried out by varying the mesh spacing Δx while keeping all other simulation parameters constant. The time-dependent pressure signal is recorded at each iteration at the point $(x, y) = (0.4, -14)$. For each simulation, the L2-norm error between the analytical and the numerical solutions is computed as follows:

$$\varepsilon = \sqrt{\frac{\int_0^T (\mathrm{Re}[\tilde{p}'] - p')^2 \mathrm{d}t}{\int_0^T \mathrm{Re}[\tilde{p}']^2 \mathrm{d}t}}.$$

The results for the evolution of ε are plotted in Fig. 8. The mesh spacing Δx ranges from 0.1 to 1.6, corresponding to 150 and 10 points per wavelength, respectively. For spatial steps between 0.8 and 1.6, the error decreases with a third-order slope. As the mesh is further refined, the convergence rate reduces to between first and second order. This behavior arises because the source terms are introduced only during the final sub-step of the Runge–Kutta cycle, rather than at every sub-step, thereby reducing the scheme's order of convergence.

C. 3D Monopole with uniform mean flow

This third configuration extends the two-dimensional case to three dimensions. Introduction of spherical waves generated by a monopolar source in a uniform flow is investigated. The monopole is located at $\boldsymbol{x}_m = (x_m, y_m, z_m)$ and is immersed in a uniform flow at $M_x = 0.8$ along the x axis. As illustrated in Fig. 9, the control surface is a cylinder centered at the origin, aligned with the x-direction, and enclosing the source, with radius $R_s = 10$ and length $L = 30$.

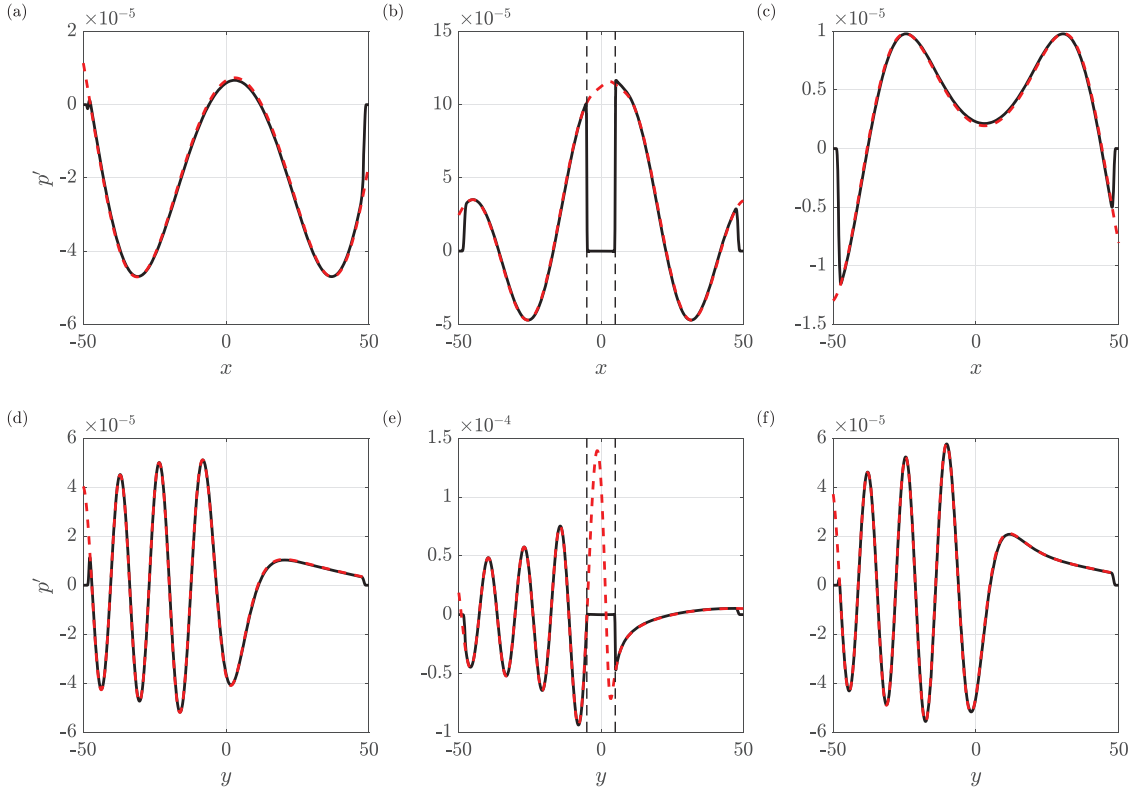

FIG. 7. Comparison between the analytical solution (dashed red line) and the numerical solution (solid black line) for a 2D monopole immersed in uniform flow at (a) $y = -30$, (b) $y = 0$, (c) $y = 30$, (d) $x = -30$, (e) $x = 0$, (f) $x = 30$. The black vertical dashed lines denote the boundaries of the surface.

https://doi.org/10.1121/10.0042388

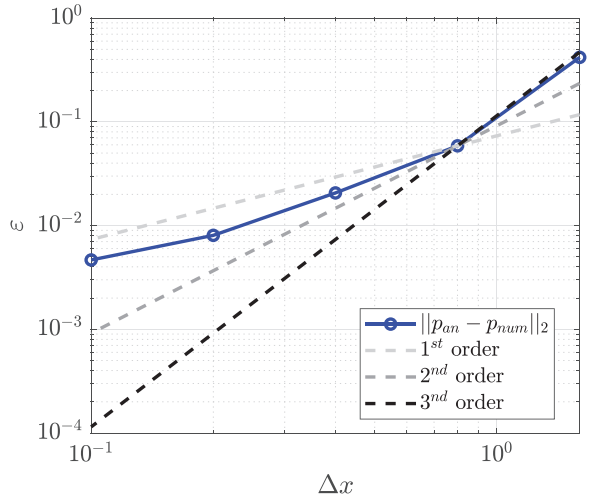

FIG. 8. L2-norm error between the numerical solution of the two-dimensional monopole case and the analytical solution, evaluated for varying mesh resolutions Δx.

The lateral surface has for equation $f(x,y,z) = \sqrt{y^2+z^2} - R_s$ for $-L/2 < x < L/2$. The unit normal vector to the lateral surface of the cylinder $\boldsymbol{n}_l$ is defined as

$$\boldsymbol{n}_l = (0,\ \sin\theta,\ \cos\theta), \tag{33}$$

where $\theta = \arctan(y/z)$ denotes the angle formed with the positive z-axis in a generic yz plane. The two bases have for equations $f(x,y,z) = \pm x - L/2$ for $\sqrt{y^2+z^2} < R_s$. The unit vectors normal to the two bases of the cylinder are defined respectively as $\boldsymbol{n}_\pm = (\pm 1, 0, 0)$.

The injection of the acoustic waves generated by a monopole source in a uniform flow relies on the corresponding analytical solution. From the velocity potential given by

$$\phi(\boldsymbol{x},t) = \frac{A}{4\pi R_1}\exp\left[-\mathrm{i}\omega\left(t - \frac{R_2}{c_0}\right)\right] \tag{34}$$

with

$$R_1 = \sqrt{(x-x_m)^2 + \beta^2[(y-y_m)^2 + (z-z_m)^2]}, \tag{35}$$

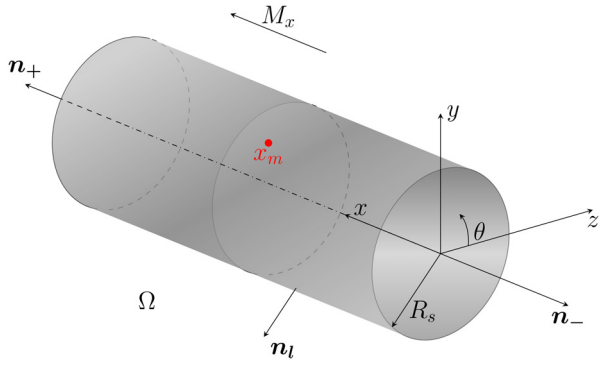

FIG. 9. Three-dimensional scheme of a cylindrical control volume V with radius R_c, enclosing an acoustic monopole located at $\boldsymbol{x}_m = (x_m, y_m, z_m)$. The configuration is immersed in a uniform flow of Mach number M_x directed along the x axis.

$$R_2 = \frac{R_1 - M_x(x - x_m)}{\beta^2}, \tag{36}$$

and $\beta^2 = 1 - M_x^2$, the acoustic pressure $\tilde{p}'$ and velocity $\tilde{\boldsymbol{u}}' = (\tilde{u}', \tilde{v}', \tilde{w}')$ can be determined as follows:

$$\tilde{p}'(\mathbf{x},t) = -\rho_0\left(\frac{\partial}{\partial t} + u_0\frac{\partial}{\partial x}\right)\phi(\mathbf{x},t), \tag{37}$$

$$\tilde{\boldsymbol{u}}'(\mathbf{x},t) = \nabla\phi(\mathbf{x},t), \tag{38}$$

with $u_0 = M_x c_0$.

The source terms can then be formulated using Eqs. (9), (12), and (13). For the lateral surface of the cylinder ($-L/2 < x < L/2$), the source terms are expressed as

$$\Lambda_\rho(\mathbf{x},t) = \rho_0\tilde{u}_n'\ \delta_b(f), \tag{39}$$

$$\Lambda_{\rho u}(\mathbf{x},t) = \rho_0 u_0\tilde{u}_n'\ \delta_b(f), \tag{40}$$

$$\Lambda_{\rho v}(\mathbf{x},t) = \tilde{p}'\sin\theta\ \delta_b(f), \tag{41}$$

$$\Lambda_{\rho w}(\mathbf{x},t) = \tilde{p}'\cos\theta\ \delta_b(f), \tag{42}$$

$$\Lambda_{\rho e_t}(\mathbf{x},t) = \left(\frac{\gamma}{\gamma-1}p_0 + \frac{1}{2}\rho_0 u_0^2\right)\tilde{u}_n'\ \delta_b(f), \tag{43}$$

where $\tilde{u}_n' = \tilde{v}'\sin\theta + \tilde{w}'\cos\theta$ denotes the velocity component in the direction normal to the lateral surface. The acoustic quantities in the source terms are those from the analytical solution on the control surface evaluated at $(x, R_s\sin\theta, R_s\cos\theta, t)$ by taking the real part.

For the bases of the cylinders with normal vectors $\boldsymbol{n}_\pm$, the source terms are given by

$$\Lambda_\rho(\mathbf{x},t) = \pm\left(\rho_0\tilde{u}' + \tilde{\rho}'u_0\right)\ \delta_b(f), \tag{44}$$

$$\Lambda_{\rho u}(\mathbf{x},t) = \pm\left(2\rho_0 u_0\tilde{u}' + \tilde{\rho}'u_0^2 + \tilde{p}'\right)\delta_b(f), \tag{45}$$

$$\Lambda_{\rho v}(\mathbf{x},t) = \pm\rho_0 u_0\tilde{v}'\,\delta_b(f), \tag{46}$$

$$\Lambda_{\rho w}(\mathbf{x},t) = \pm\rho_0 u_0\tilde{w}'\,\delta_b(f), \tag{47}$$

$$\Lambda_{\rho e_t}(\mathbf{x},t) = \pm\left[\frac{\gamma}{\gamma-1}(\tilde{p}'u_0 + p_0\tilde{u}') + \frac{3}{2}\rho_0 u_0^2\tilde{u}' + \frac{1}{2}\tilde{\rho}'u_0^3\right]\ \delta_b(f). \tag{48}$$

Once again, the imposed acoustic quantities on the control surfaces are evaluated at $(x = \pm L/2, y, z, t)$.

The monopole amplitude A is set to 10^{-3} and the angular frequency $\omega = 0.314$. The grid spacing is set to $\Delta x = 0.25$, providing 24 points per wavelength in the upstream-propagating wave region. The computational domain consists of $401 \times 281 \times 461$ points in the x, y, and z directions, respectively. The solution is computed up to $t = 200$. The computational cost of the simulation is 6 h of wall-clock time on a single compute node utilizing 32 OpenMP threads.

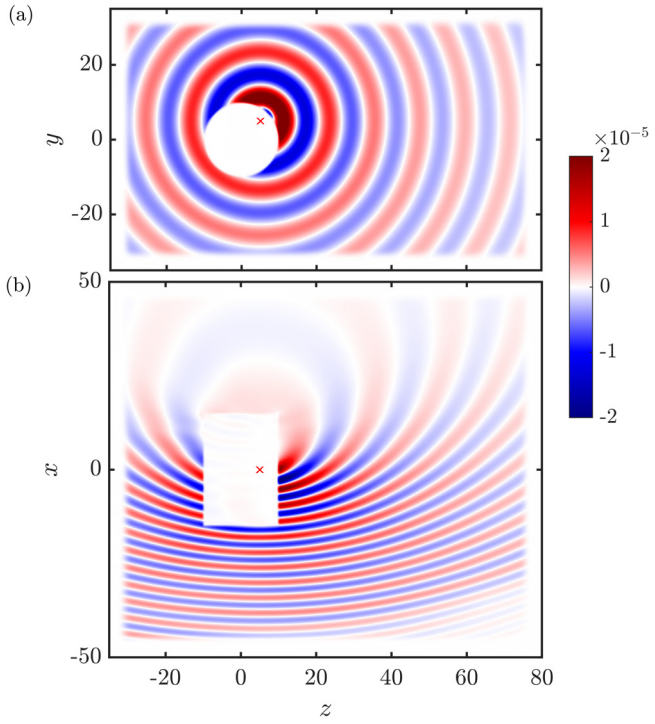

FIG. 10. Pressure field generated by a three-dimensional monopole immersed in a uniform flow with Mach number $M_x = 0.8$ at $t = 200$ on (a) the yz-plane at $x = 0$ and (b) the xz-plane at $y = 0$. The monopole, indicated by the red cross, is located at $(x_m, y_m, z_m) = (0, 5, 5)$ within a cylindrical control surface centered at the origin with radius $R_s = 10$.

The acoustic pressure signal at the final time step is shown in Figs. 10(a) and 10(b) on the yz and xz planes, respectively. The control surface boundaries are clearly identifiable. The time evolution of the pressure fluctuation field can be seen in Mm. 3.

Mm. 3. Evolution of the pressure field for a three-dimensional monopole with a uniform flow $M_x = 0.8$ along the x axis enclosed in a cylindrical surface.

A comparison between the analytical and numerical solutions is provided in Fig. 11, evaluated on the xz-plane at $y = 0$ in Figs. 11(a)–11(c), on the yz-plane at $x = 0$ in Figs. 11(d)–11(f) and on the xy-plane at $z = 0$ in Figs. 11(g)–11(i). The numerical results closely match the analytical solution in both phase and amplitude.

D. Open fan

An application to a R&T Rotor/Stator open-fan configuration is finally considered. This architecture is of interest for its potential to reduce fuel consumption, compared to ultra-high bypass ratio engines. However, the absence of a nacelle necessitates an evaluation of the shock-wave propagation generated at the rotor blade tips. Several studies have addressed open-rotor applications. Daydé-Thomas *et al.*[17] proposed a tonal noise model based on the FWH analogy using Goldstein's formulation. A tonal noise study was carried out by Lewis *et al.*[18] using a hybrid approach that couples a Reynolds-averaged Navier-Stokes (RANS) simulation with the FWH integral formulation. An open test case for an open-fan engine was proposed by Greco *et al.*,[19] providing a cross-comparison of RANS results obtained with different CFD solvers. To the authors' knowledge, no previous studies have investigated non-linear effects in the propagation of shock-waves for open-fan configurations.

In the present study, the conservative variables field introduced into the computational domain is extracted from

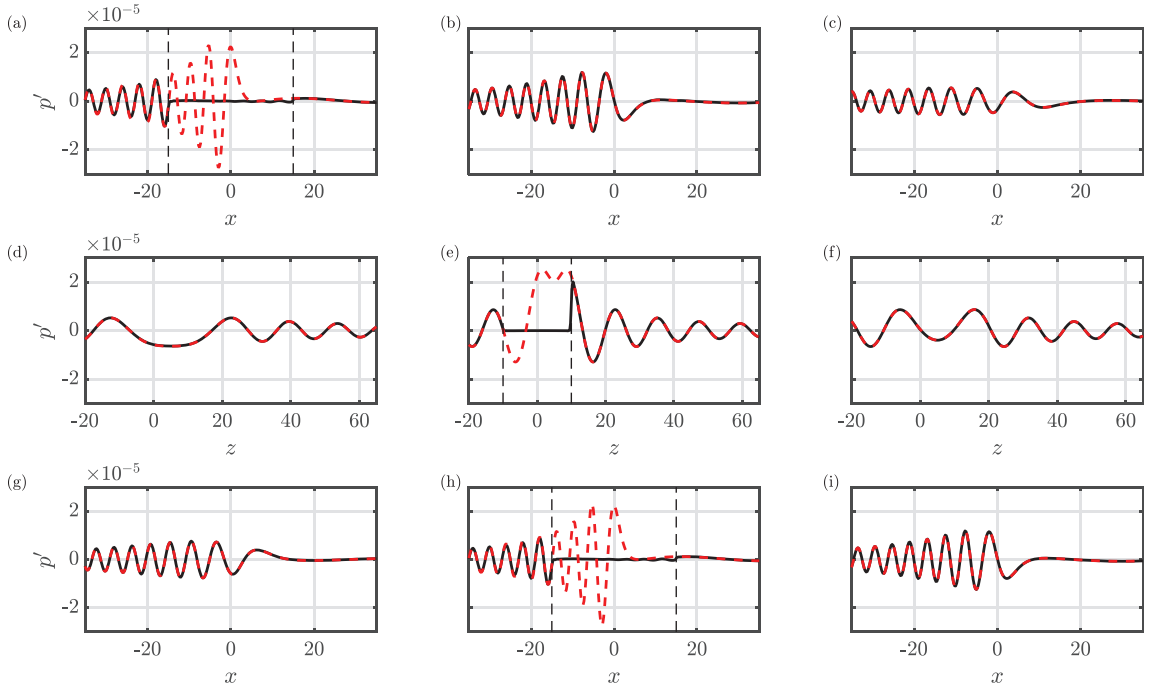

FIG. 11. Comparison between the analytical solution (dashed red line) and the numerical solution (solid black line) in the xz-plane at $y = 0$ for (a) $z = 0$, (b) $z = 20$, (c) $z = 40$, in the yz-plane at $x = 0$ for (d) $y = -20$, (e) $y = 0$, (f) $y = 20$, and in the xy-plane at $z = 0$ for (g) $y = -20$, (h) $y = 0$, (i) $y = 20$. The black vertical dashed lines denotes the boundaries of the surface.

https://doi.org/10.1121/10.0042388

a RANS simulation, performed in a configuration where only the rotor is present. The CFD simulation is carried out using the elsA CFD solver.[20] The calculation is performed on a single blade-passage rotor-alone configuration, which is then reconstructed over 360° by applying periodicity in the azimuthal direction. The resulting signal is interpolated onto a cylindrical control surface of radius $R_s = 1.3R$, where R denotes the rotor radius. The rotor plane lies in the plane $x = 0$. The perturbation field $(\rho', (\rho u_i)', (\rho e_t)', p')$ at each point on the cylindrical surface is computed by subtracting the azimuthal mean from the conservative variables extracted from the RANS simulation. The source terms are computed using the same formulation described in Sec. IV C. The reference frame coincides with that shown in Fig. 9, and the simulation is conducted under cruise conditions, with a uniform flow M_x aligned along the x axis and no incidence.

The cylindrical surface is shown in Fig. 12. Since the RANS simulation is performed on a single blade sector, the resulting signal is periodic. This signal is then rotated around the x axis of the cylindrical surface according to the rotor's angular velocity, defined as $\Omega = \Delta\theta/\Delta t$, where $\Delta\theta$ is the angular displacement per time step Δt. Two complete rotations are performed in the simulation. The computational domain consists of $241 \times 255 \times 334$ points in the x, y, and z directions, respectively, with 24 points per wavelength in the upstream-propagating wave region. The computational cost of the simulation is 4 h of wall-clock time on a single compute node utilizing 32 OpenMP threads.

The resulting acoustic pressure field generated by the source terms distributed along the cylindrical surface is shown in Fig. 13. The signal primarily propagates outward from the cylindrical surface and is subsequently absorbed by the PML at the domain boundaries. Due to the presence of a uniform flow M_x, the acoustic waves undergo upstream propagation against the flow direction and experience a wavelength increase in the downstream direction. However, a small portion of the signal penetrates into the surface. This effect is likely attributable to the fact that the source signal is extracted directly from a RANS simulation, rather than being analytically defined as in the previous more academic

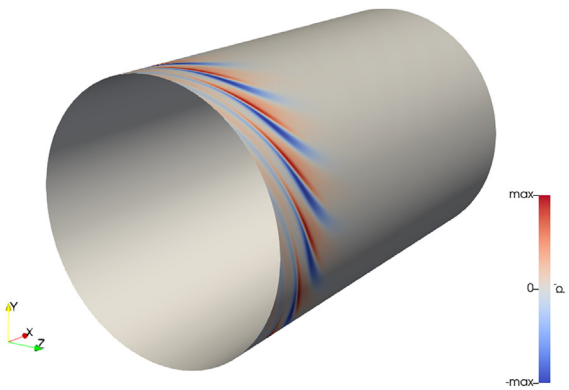

FIG. 12. Isometric view of the pressure oscillations field generated by an open fan rotor on a cylindrical control surface.

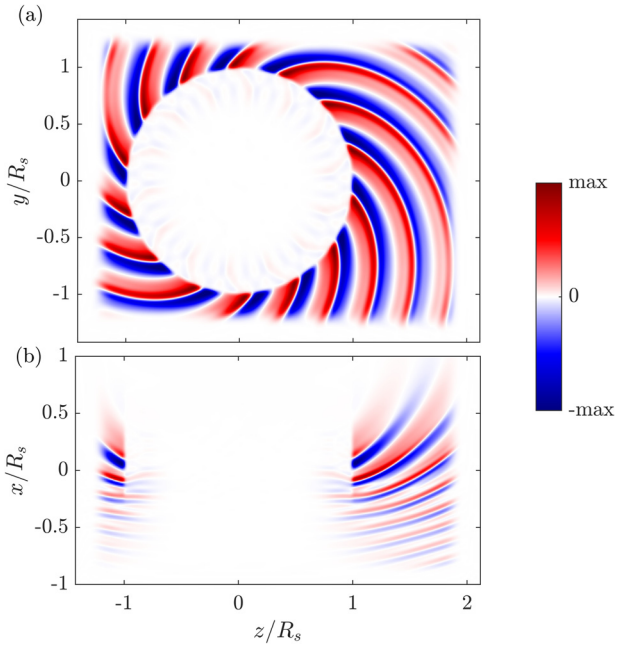

FIG. 13. Pressure field generated by an open fan rotor in (a) the yz-plane and (b) the xz-plane.

cases. Nevertheless, this does not compromise the validity of the results, as demonstrated by the comparison with the FWH method for sound pressure level (SPL) computation on the xz-plane, presented in Fig. 14. The highest SPL is observed in the vicinity of the rotor plane at $x/R_s = 0$ and gradually decreases upstream and downstream, as well as along z.

A more quantitative comparison between the two approaches is presented in Fig. 15. The SPL is plotted along three lines on the xz-plane at $y = 0$, corresponding to normalized vertical positions $z/R_s = 1.03$, 1.41, and 1.72 in Figs. 15(a), 15(b), and 15(c), respectively. Three additional simulations are performed by introducing a scaling factor α multiplying the amplitude of the source terms to assess the influence of non-linear effects. The values $\alpha = 0.5$, 0.1, and

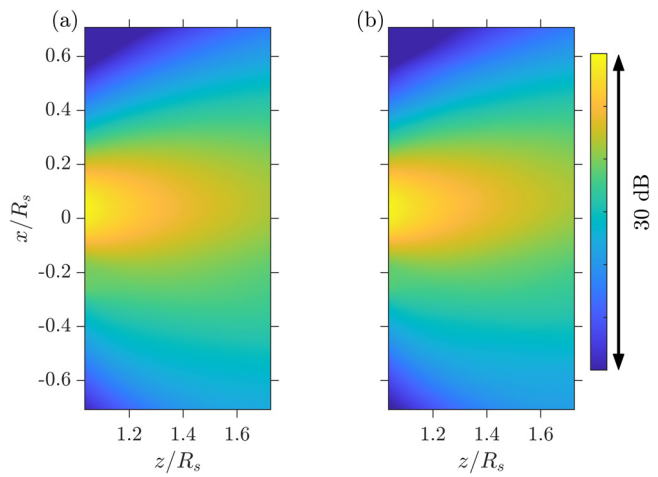

FIG. 14. SPL in the xz-plane at $y = 0$ for (a) the Ffowcs Williams-Hawkings integral formulation and (b) the present method.

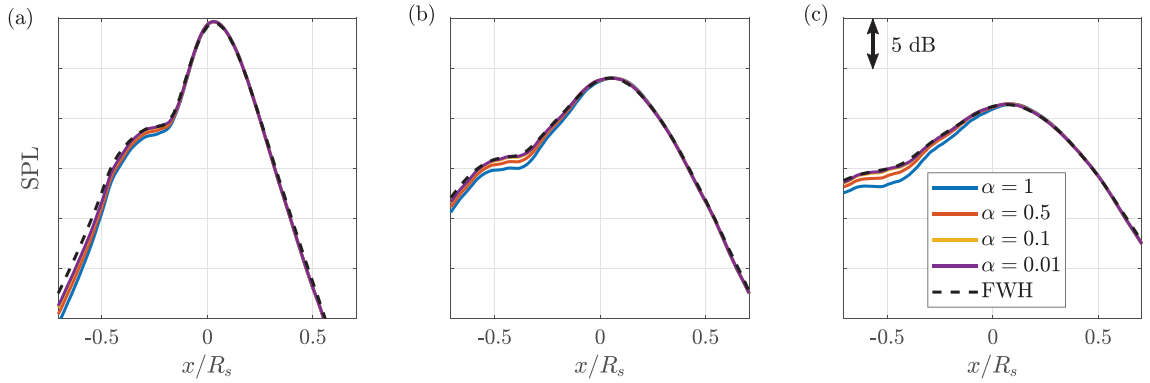

FIG. 15. Normalized comparison of the Sound Pressure Level between the Ffowcs Williams-Hawkings integral formulation in dashed line, and the present method at $z/R_s = 1.03$ (a), 1.41 (b), and 1.72 (c) for different values of α.

0.01 are selected to progressively suppress non-linear propagation effects. The baseline simulation uses unmodified source terms and therefore corresponds to $\alpha = 1$. For each simulation, the SPL is computed and normalized using the corresponding value of α, enabling a direct comparison across all cases. Downstream of the rotor, for $x > 0$, the results are identical for all simulations, with complete overlap between the Euler and the FWH curves. Upstream of the rotor, for $x < 0$, the Euler solution progressively approaches the FWH prediction as α decreases. Convergence is achieved for $\alpha = 0.1$, below which non-linear attenuation of the SPL is no longer observed. Non-linear effects are therefore confined to the region $x/R_s < 0.2$, upstream of the engine. This behavior can be explained by the shock formation distance $\bar{x}$ in the presence of a uniform flow,[21,22] defined as the distance required for a sinusoidal plane wave to first present a vertical tangent. Relative to a quiescent medium, this distance decreases for waves propagating against the flow and increases for waves propagating with the flow. For the configuration considered here, the theoretical shock formation distance is $\bar{x}/R_s = 0.18$ for waves propagating against the flow, whereas it reaches $\bar{x}/R_s = 11$ for waves propagating in the direction of the flow.

V. CONCLUSION

The method proposed in this study enables the injection of acoustic waves through volumetric source terms distributed along an arbitrary control surface. This non-linear formulation is rigorously derived from fluid mechanics equations to keep them very general. Validation has been carried out for oblique plane waves on a Cartesian grid and for a monopole source in both two and three dimensions under uniform flow and with a cylindrical volume control on a Cartesian mesh. In all cases, the results showed excellent agreement by comparison with corresponding analytical solutions.

The source terms are immersed in the computational mesh, avoiding the need to conform the mesh to the control surface geometry. Mesh refinement near the control surface may be required to properly take into account its shape. The authors recommend the use of compact sources by selecting a Gaussian half-width equal to the mesh spacing. Future work could investigate the numerical error obtained using a uniform Cartesian mesh compared with that from a mesh conforming to the geometry of the control surface.

Finally, the method was also applied to an open fan configuration. The comparison of the radiated pressure field with the Ffowcs Williams–Hawkings integral formulation is again in very good agreement. Unlike the FWH approach, the present method allows the inclusion of non-linear effects, as it is based on solving the non-linear Euler equations.

Building on these findings, the proposed method offers several notable advantages. It can be directly applied on a uniform Cartesian mesh, regardless of the chosen control surface, which greatly simplifies implementation in finite-difference solvers. Because the control surface is fully immersed within the computational domain, no boundary conditions need to be imposed and no mesh adaptation to the surface geometry is required. Unlike characteristic-based wave-injection techniques, the present approach does not require the evaluation of additional terms: only volumetric source terms are added within the Runge–Kutta loop, leaving the computational cost essentially unchanged. Care must be taken to ensure an adequate level of source compactness relative to the mesh resolution, but this requirement is straightforward to satisfy. Overall, the method provides a robust and efficient alternative for CFD/CAA coupling, being also capable of capturing non-linear propagation effects.

ACKNOWLEDGMENTS

This material is based upon work supported by the ANRT (Association nationale de la recherche et de la technologie) with a CIFRE fellowship granted to G.C. The study was performed within the framework of the industrial chair ARENA (ANR-18-CHIN-0004-01) co-financed by Safran Aircraft Engines and the French National Research Agency (ANR), and within the framework of the LABEX CeLyA (ANR-10-LABX-0060) of Université de Lyon, within the program "Investissements d'Avenir" (ANR-16-IDEX-0005) operated by the French National Research Agency (ANR). This work was granted access to the HPC

https://doi.org/10.1121/10.0042388

resources of PMCS2I (Pôle de Modélisation et de Calcul en Sciences de l'Ingénieur de l'Information) of the École Centrale de Lyon, Écully, France.

AUTHOR DECLARATIONS

Conflict of Interest

The authors have no conflicts to disclose.

DATA AVAILABILITY

Data available on request from the authors.

APPENDIX A: CONVOLUTION

The calculation of the convolution in Eq. (25) is detailed below. Complex notation is used to simplify the calculations. The convolution writes explicitly as

$$p'(x,y,t) = \int\int\int\int_{-\infty}^{+\infty} g_0(x-x', y-y', z-z', t-t') \times S(x',y',t')\,\mathrm{d}x'\mathrm{d}y'\mathrm{d}z'\mathrm{d}t', \tag{A1}$$

where g_0 is the Green function in free field

$$g_0(x,y,z,t) = \frac{1}{4\pi R}\delta(t - R/c_0) \tag{A2}$$

with $R = \sqrt{x^2+y^2+z^2}$. The term S is given by $S = S_1 + S_2$ with

$$S_1 := \frac{\partial \Lambda_\rho}{\partial t} = -\mathrm{i}k_x A \exp(-\mathrm{i}\omega t + \mathrm{i}k_y y)\ \delta_b(x), \tag{A3}$$

$$S_2 := -\nabla\cdot\Lambda_{\rho u} = -A\exp(-\mathrm{i}\omega t + \mathrm{i}k_y y)\ \delta_b'(x) \tag{A4}$$

with $k_x = k_0\cos\theta$ and $k_y = k_0\sin\theta$. $\delta_b(x)$ is the normalized Gaussian distribution defined by Eq. (15) and $\delta_b'(x)$ is its derivative. For the sake of clarity, the integral is calculated by separating the two addends.

Calculation for S_1. The convolution between the Green's function g_0 and S_1 reads

$$p_1(x,y,t) = \int\int\int\int_{-\infty}^{+\infty} \frac{1}{4\pi R}\ \delta\left(t - t' - \frac{R}{c_0}\right) \times S_1(x',y',z',t')\ \mathrm{d}x'\ \mathrm{d}y'\ \mathrm{d}z'\ \mathrm{d}t'.$$

The property of the Dirac distribution is used for integration over time by evaluating S_1 at $t' = t - R/c_0$

$$p_1 = -A\frac{\mathrm{i}k_x}{\sqrt{\pi}b}\int_{-\infty}^{+\infty}\exp\left[-\frac{x'^2}{b^2}\right] \times \int\int_{-\infty}^{+\infty}\frac{\exp\left(-\mathrm{i}\omega t + \mathrm{i}k_0 R + \mathrm{i}k_y y'\right)}{4\pi R}\,\mathrm{d}y'\,\mathrm{d}z'\,\mathrm{d}x'. \tag{A5}$$

The resolution of the double integral is given in detail in Appendix B. Equation (B3) is used and the integral reads

$$p_1 = \frac{B}{2\sqrt{\pi}b}\int_{-\infty}^{+\infty}\exp\left[-\frac{x'^2}{b^2}\right]\exp\left(\mathrm{i}k_x\ |x-x'|\right)\ \mathrm{d}x' \tag{A6}$$

with $B = A\exp(-\mathrm{i}\omega t + \mathrm{i}k_y y)$.

The assumption is made to be in the far field, i.e., $|x| \gg b$. At the first order, one obtains

$$|x-x'| \approx |x|\left(1 - \frac{x'}{x}\right) = |x| - x'\ \mathrm{sign}(x). \tag{A7}$$

Equation (A6) is then written as

$$p_1 = \frac{B}{2\sqrt{\pi}b}\exp(\mathrm{i}k_x|x|)\int_{-\infty}^{+\infty}\exp\left(-\frac{x'^2}{b^2}\right) \times \exp[-\mathrm{i}k_x x'\ \mathrm{sign}(x)]\ \mathrm{d}x'. \tag{A8}$$

The integral in the above equation corresponds to the Fourier transform of the Gaussian function, that is given by[23]

$$\int_{-\infty}^{+\infty}\exp\left(-q^2x^2\right)\exp(\mathrm{i}px)\mathrm{d}x = \frac{\sqrt{\pi}}{q}\exp\left(-\frac{p^2}{4q^2}\right) \tag{A9}$$

for p and q real numbers. Equation (A9) is used in Eq. (A8) leading to

$$p_1 = \frac{B}{2\sqrt{\pi}b}\exp(\mathrm{i}k_x|x|)\sqrt{\pi}b\exp\left(-\frac{k_x^2b^2}{4}\right) = \frac{A_b}{2}\exp\left(-\mathrm{i}\omega t + \mathrm{i}k_x|x| + \mathrm{i}k_y y\right) \tag{A10}$$

with

$$A_b = A\exp\left(-\frac{k_x^2b^2}{4}\right). \tag{A11}$$

Calculation for S_2. The convolution between the Green's function g_0 and S_2 reads

$$p_2(x,y,t) = \frac{2A\exp(-i\omega t)}{\sqrt{\pi}b^3}\int_{-\infty}^{+\infty}x'\exp\left(-\frac{x'^2}{b^2}\right) \times \int\int_{-\infty}^{+\infty}\frac{\exp\left(\mathrm{i}k_0 R + \mathrm{i}k_y y'\right)}{4\pi R}\mathrm{d}x'\ \mathrm{d}y'\ \mathrm{d}z',$$

where the Dirac distribution property is used for the integration in time.

Once again, Eq. (B3) is used to solve the double integral

$$p_2 = C\int_{-\infty}^{+\infty}x'\exp\left(\mathrm{i}k_x|x-x'| - \frac{x'^2}{b^2}\right)\ \mathrm{d}x'$$

with $C = \mathrm{i}A\exp(-\mathrm{i}\omega t + \mathrm{i}k_y y)/\left(k_x\sqrt{\pi}b^3\right)$. The same first order approximation as in Eq. (A7) is made:

$$p_2 = C\exp(\mathrm{i}k_x|x|)\int_{-\infty}^{+\infty} x'\exp\left(-\frac{x'^2}{b^2}\right) \times \exp\left(-\mathrm{i}k_x x'\mathrm{sign}(x)\right)\,\mathrm{d}x'. \quad \text{(A12)}$$

The integral above corresponds to the Fourier transform of the derivative of the Gaussian function. It can be written as

$$\int_{-\infty}^{+\infty} x\exp(-q^2x^2)\exp(\mathrm{i}px)\,\mathrm{d}x = \frac{\mathrm{i}p}{2q^2}\frac{\sqrt{\pi}}{q}\exp\left(-\frac{p^2}{4q^2}\right)$$

for p and q real numbers. After appropriate simplifications, the pressure field generated by the source term S_2 is finally obtained

$$p_2 = \frac{A_b}{2}\mathrm{sign}(x)\exp\left(-\mathrm{i}\omega t + \mathrm{i}k_x|x| + \mathrm{i}k_y y\right). \quad \text{(A13)}$$

Total acoustic pressure field. The acoustic pressure field generated by S_1 and S_2 is calculated by the sum of Eqs. (A10) and (A13), i.e., $p' = p_1 + p_2$, yielding

$$p'(x,y,t) = A_b H(x)\exp(-\mathrm{i}\omega t + \mathrm{i}k_x x + \mathrm{i}k_y y). \quad \text{(A14)}$$

Taking the real part of the equation above leads to Eq. (25).

APPENDIX B: INTEGRAL CALCULATION

In this appendix, we detail the calculation of the integral

$$I(x,x',y) = \int\int_{-\infty}^{+\infty} \frac{\exp\left(\mathrm{i}k_0 R + \mathrm{i}k_y y'\right)}{4\pi R}\mathrm{d}y'\mathrm{d}z' \quad \text{(B1)}$$

with $R = \sqrt{\rho^2 + z'^2}$ and $\rho^2 = (x-x')^2 + (y-y')^2$.

We first use the relation

$$\int_{-\infty}^{+\infty} \frac{\exp(\mathrm{i}k_0 R)}{4\pi R}\mathrm{d}z' = \frac{\mathrm{i}}{4}H_0^{(1)}(k_0\rho),$$

where $H_0^{(1)}$ is the Hankel function of the first kind, which can be derived from Eqs. (3.714.2) and (3.714.3) in Gradshteyn and Ryzhik.[23] With this relation, Eq. (B1) becomes

$$I = D\int_{-\infty}^{+\infty} H_0^{(1)}\left(k_0\sqrt{\chi^2 + y''^2}\right)\exp\left(-\mathrm{i}k_y y''\right)\,\mathrm{d}y''$$

with $D = \mathrm{i}\exp(\mathrm{i}k_y y)/4$, $\chi = x - x'$, and $y'' = y - y'$. By splitting the integral into $(-\infty, 0]$ and $[0, +\infty)$, it can be written as

$$I = 2D\int_{0}^{+\infty} H_0^{(1)}\left(k_0\sqrt{\chi^2 + y''^2}\right)\cos(k_y y'')\,\mathrm{d}y''. \quad \text{(B2)}$$

Using Eqs. (6.677.3) and (6.677.4) in Gradshteyn and Ryzhik,[23] it can be shown that

$$\int_{0}^{+\infty} H_0^{(1)}\left(\alpha\sqrt{x^2+z^2}\right)\cos(\beta x)\,\mathrm{d}x = \frac{\exp\left(\mathrm{i}|z|\sqrt{\alpha^2-\beta^2}\right)}{\sqrt{\alpha^2-\beta^2}}$$

for $0 < \beta < \alpha$ and for z a real number. Using the above equation in Eq. (B2) allows us to obtain

$$I(x,x',y) = \frac{\mathrm{i}}{2k_x}\exp\left(\mathrm{i}k_x\,|x-x'| + \mathrm{i}k_y y\right). \quad \text{(B3)}$$

[1]X. Gloerfelt and J.-C. Robinet, "Silent inflow condition for turbulent boundary layers," Phys. Rev. Fluids **2**, 124603 (2017).
[2]J. E. Ffowcs Williams and D. L. Hawkings, "Sound generation by turbulence and surfaces in arbitrary motion," Philos. Trans. R. Soc. London, Ser. A: Math. Phys. Sci. **264**(1151), 321–342 (1969).
[3]X. Gloerfelt, C. Bailly, and D. Juvé, "Direct computation of the noise radiated by a subsonic cavity flow and application of integral methods," J. Sound Vib. **266**(1), 119–146 (2003).
[4]N. de Cacqueray and C. Bogey, "Noise of an overexpanded Mach 3.3 jet: Non-linear propagation effects and correlations with flow," Int. J. Aeroacoust. **13**(7-8), 607–632 (2014).
[5]A. Emmanuelli, D. Dragna, S. Ollivier, and P. Blanc-Benon, "Characterization of topographic effects on sonic boom reflection by resolution of the Euler equations," J. Acoust. Soc. Am. **149**(4), 2437–2450 (2021).
[6]A. Langenais, F. Vuillot, C. Peyret, G. Chaineray, and C. Bailly, "Assessment of a two-way coupling methodology between a flow and a high-order nonlinear acoustic unstructured solvers," Flow. Turbul. Combust. **101**, 681–703 (2018).
[7]K. W. Thompson, "Time dependent boundary conditions for hyperbolic systems," J. Comput. Phys. **68**(1), 1–24 (1987).
[8]K. W. Thompson, "Time-dependent boundary conditions for hyperbolic systems II," J. Comput. Phys. **89**(2), 439–461 (1990).
[9]T. J. Poinsot and S. K. Lele, "Boundary conditions for direct simulations of compressible viscous flows," J. Comput. Phys. **101**(1), 104–129 (1992).
[10]G. Daviller, G. Oztarlik, and T. Poinsot, "A generalized non-reflecting inlet boundary condition for steady and forced compressible flows with injection of vortical and acoustic waves," Comput. Fluids **190**, 503–513 (2019).
[11]M. Daroukh, C. Polacsek, and A. Chelius, "Shock wave generation and radiation from a turbofan engine under flow distortion," AIAA J. **58**(2), 787–801 (2020).
[12]F. Nicoud, "Defining wave amplitude in characteristic boundary conditions," J. Comput. Phys. **149**(2), 418–422 (1999).
[13]T. Colonius, "Modeling artificial boundary conditions for compressible flow," Annu. Rev. Fluid Mech. **36**, 315–345 (2004).
[14]K. Maeda and T. Colonius, "A source term approach for generation of one-way acoustic waves in the Euler and Navier–Stokes equations," Wave Motion **75**, 36–49 (2017).
[15]C. Bogey and C. Bailly, "A family of low dispersive and low dissipative explicit schemes for flow and noise computations," J. Comput. Phys. **194**(1), 194–214 (2004).
[16]F. Q. Hu, "Development of PML absorbing boundary conditions for computational aeroacoustics: A progress review," Comput. Fluids **37**(4), 336–348 (2008).
[17]V. Daydé-Thomas, C. Polacsek, S. Fauqueux, X. Gloerfelt, and J. Marjono, "Tone noise characterization of an open-fan engine using source-mode integral formulations," in *30th AIAA/CEAS Aeroacoustics Conference* (2024).
[18]D. Lewis, C. Perrin, and F. Falissard, "Tonal noise predictions of a generic open-fan based on a hybrid URANS approach," in *30th AIAA/CEAS Aeroacoustics Conference* (2024).
[19]M. Greco, R. Corral, F. Zhao, R. Schnell, C. Rovira Sala, R. Martinez Luque, and F. Gea-Aguilera, "An open virtual test case for open fans," J. Turbomach. **148**, 061019 (2026).
[20]L. Cambier, S. Heib, and S. Plot, "The Onera elsA CFD software: Input from research and feedback from industry," Mech. Industry **14**, 159–174 (2013).
[21]A. Polyakova, "Plane sound wave of finite amplitude in a moving medium," Dokl. Akad. Nauk. Russ. Acad. Sci. **137**, 1347–1349 (1961).
[22]A. Nayfeh, B. Shaker, and J. Kaiser, "Computation of nonlinear one-dimensional waves in near-sonic flows," AIAA J. **16**(11), 1154–1159 (1978).
[23]I. S. Gradshteyn and I. M. Ryzhik, *Table of Integrals, Series, and Products*, 7th ed. (Academic Press, New York, 2007).